npj | Quantum Materials

www.nature.com/npjquantmats

ARTICLE OPEN

Unconventional spin-phonon coupling via the Dzyaloshinskii–Moriya interaction

Jaeseok Son[1,2], Byung Cheol Park[1,2], Choong H. Kim[1,2], Hwanbeom Cho[1,2], So Yeun Kim[1,2], Luke J. Sandilands[1,2,5], Changhee Sohn[3], Je-Geun Park[1,2], Soon Jae Moon[4] and Tae Won Noh[1,2]

Spin-phonon coupling (SPC) plays a critical role in numerous intriguing phenomena of transition metal oxides (TMOs). In *3d* and 4*d* TMOs, the coupling between spin and lattice degrees of freedom is known to originate from the exchange interaction. On the other hand, the origin of SPC in 5*d* TMOs remains to be elucidated. To address this issue, we measured the phonon spectra of the 5*d* pyrochlore iridate $Y_2Ir_2O_7$ using optical spectroscopy. Three infrared-active phonons soften below the Néel temperature of $T_N \approx 170$ K, indicating the existence of strong SPC. Simulations using density functional theory showed that the coupling is closely related to the Ir–O–Ir bond angle. A tight-binding model analysis reveals that this SPC is mainly mediated by the Dzyaloshinskii–Moriya interaction rather than the usual exchange interaction. We suggest that such unconventional SPC may be realized in other 5*d* TMOs with non-collinear magnetic order.

npj Quantum Materials (2019)4:17 ; https://doi.org/10.1038/s41535-019-0157-0

INTRODUCTION

The coupling between various degrees of freedom (spin, charge, lattice, and orbital) is an important paradigm in condensed matter physics. Such couplings are known to give rise to novel ground states and various emergent phenomena,[1–5] including high T_C superconductivity,[2,3] colossal magnetoresistance,[4] etc. Recently, there has been increasing interest in spin-phonon coupling (SPC) within the context of multiferroics and spintronics.[5–9] In multiferroic materials, SPC has been invoked to explain intriguing phenomena such as the thermal Hall effect[8] while it also determines the spin relaxation time in spintronics applications.[9] Moreover, SPC presents the opportunity to engineer new functionality in transition metal oxides (TMOs). For example, it is possible to stabilize a specific magnetic ground state with epitaxial strain[10] or generate magnetoelastic effects by changing the magnetic easy-axis.[7] In this context, it has become increasingly important to develop a detailed understanding of SPC.

In general, we can describe the physics of most spin-related phenomena in solids using the spin Hamiltonian (H_{spin}). This can be written as a sum of the isotropic exchange (IE) interaction, the Dzyaloshinskii–Moriya (DM) interaction, the anisotropic exchange (AE) interaction, and the single-ion anisotropy (SIA):[11–13]

$$H_{\mathrm{spin}} = \sum_{ij}^{\mathrm{nn}} \left[J_{\mathrm{IE}} \left(\mathbf{S}_i \cdot \mathbf{S}_j \right) + \mathbf{D}_{ij} \cdot \left(\mathbf{S}_i \times \mathbf{S}_j \right) + \mathbf{S}_i \cdot \mathbf{\Gamma}_{ij} \cdot \mathbf{S}_j \right] + A \sum_i (\mathbf{n}_i \cdot \mathbf{S}_i)^2, \quad (1)$$

where J_{IE}, $\mathbf{D}_{ij}$, and $\mathbf{\Gamma}_{ij}$ are the coefficients of the IE, DM, and AE interactions, respectively. A and $\mathbf{n}_i$ are the coefficient of the SIA and the direction vector of corresponding easy-axis. $\mathbf{S}_i$ and $\mathbf{S}_j$ are the spins at the nearest neighboring i^{th} and j^{th} sites.[14,15] Spin interactions are mediated by the Coulomb interaction of electrons at neighboring sites[16] and are highly dependent on the positions of the neighboring ions. Consequently, J_{IE}, $\mathbf{D}_{ij}$, $\mathbf{\Gamma}_{ij}$ and/or A terms can be dynamically modulated by a lattice vibration, resulting in SPC and a renormalization of the phonon frequencies.

A large number of studies have focused on 3*d* and 4*d* TMOs[17–29] where the SPC may be explained in terms of dynamic modulation of the IE interaction. $R MnO_3$ (*R*: rare-earth site ion), one of the widely investigated 3*d* TMOs, shows strong SPC phenomena which is closely linked with multiferroicity.[17–23] Geometrically frustrated TMOs are also known to have strong SPC.[24–27] For example, in 3*d* ACr_2O_4 (*A*: Cd, Zn), the coupling leads to spin-driven Jahn-Teller effects which relieve the magnetic frustration.[24–26] Similarly, strong SPC could occur also in 4*d* $Y_2Ru_2O_7$ and $Y_2Mo_2O_7$ with spin-glass state.[27,28] All of these SPC phenomena have been well explained by the dynamic modulation of the IE interaction.[17–29]

The H_{spin} in Eq. (1) indicates that other magnetic interactions could also induce SPC, but such possibilities have not been investigated to date. Recently, the DM interaction has attracted significant attention due to its critical role in multiferroics[30,31] and topological materials.[32] It is therefore highly desirable to explore the possibility of novel SPC mediated via the DM interaction. Equation (1) shows that such an alternative mechanism requires that both $\mathbf{D}_{ij}$ and $\langle \mathbf{S}_i \times \mathbf{S}_j \rangle$ be large. It should be noted that the DM interaction term originates from spin-orbit coupling (SOC).[14] The SOC is the relativistic interaction that increases roughly with Z^2 (Z: atomic number).[33] For example, the SOC of 5*d* TMOs is about 500 meV, much larger than that of 3*d* TMOs (typically <10 meV). Therefore, compounds containing heavy elements are better candidates to search for unconventional SPC based on strong SOC.

Among 5*d* TMOs, pyrochlore iridates are good candidates to search for new types of SPC. First, they have an intriguing ground

[1]Center for Correlated Electron Systems, Institute for Basic Science (IBS), Seoul 08826, Korea; [2]Department of Physics and Astronomy, Seoul National University, Seoul 08826, Korea; [3]Department of Physics, Ulsan National Institute of Science and Technology, Ulsan 44919, Korea; [4]Department of Physics, Hanyang University, Seoul 04763, Korea; [5]Present address: Metrology Research Centre, National Research Council of Canada, 1200 Montreal Road, Ottawa, ON K1A 0R6, Canada
Correspondence: Tae Won Noh (twnoh@snu.ac.kr)

Received: 1 January 2019 Accepted: 2 April 2019
Published online: 29 April 2019

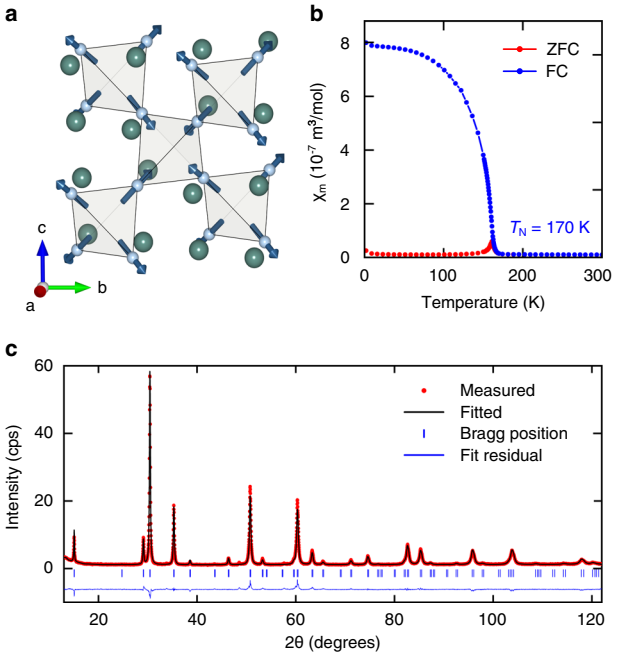

Fig. 1 Sample characterization of pyrochlore iridate $Y_2Ir_2O_7$. **a** Lattice and magnetic structure of pyrochlore iridates. The pyrochlore lattice has a corner-sharing tetrahedral structure. The large green spheres show the positions of the Y ions, and Ir ions are located at the corner of each tetrahedron. O ion positions are not displayed, for simplicity. With the all-in-all-out (AIAO) antiferromagnetic order, all Ir spins at the corner of one tetrahedron point inward into the center of the tetrahedron, while those at the neighboring tetrahedra point outward. **b** The $\chi_m(T)$ graphs of the $Y_2Ir_2O_7$ polycrystalline sample at $H = 0.1$T for field cooling (FC) and zero field cooling (ZFC). **c** Powder X-ray diffraction data for $Y_2Ir_2O_7$. The blue bars indicate the positions of the Bragg peaks from the Rietveld refinement

state, called $J_{\text{eff}} = 1/2$ state,[15,34] due to strong SOC. Second, pyrochlore iridates host an intriguing form of antiferromagnetism, namely the all-in-all-out (AIAO) magnetic order.[32,35] As shown in Fig. 1a, all spins of one (neighboring) tetrahedron point inward (outward).[36] This non-collinear spin configuration results in a large $\langle \mathbf{S}_i \times \mathbf{S}_j \rangle$ value in equation (1). Significant dynamic modulation of the DM interaction can therefore lead to a renormalization of the phonon frequencies which cannot be fully explained by the IE interaction alone.

To investigate SPC with the AIAO magnetic order, we focused on polycrystalline samples of $Y_2Ir_2O_7$. In Fig. 1b, the magnetic susceptibility of this compound clearly indicates antiferromagnetic ordering at Néel temperature $T_N \approx 170$ K. We verified the crystal structure of our sample using X-ray diffraction (XRD), as shown in Fig. 1c. The good agreement between experimental XRD results and the Rietveld refinement fitting confirmed the pyrochlore structure of our sample.

The phonon renormalization due to SPC can be directly measured by infrared (IR) spectroscopy.[11] In general, SPC phenomena have been widely investigated by measuring anomalies in spin wave dispersion with either neutron or X-ray scattering experiments.[37,38] However, in $Y_2Ir_2O_7$ the constituent Ir ions strongly absorb neutrons, making neutron scattering experiments difficult. Resonant inelastic X-ray scattering experiments could be another option, but the precise analysis of anomalies due to SPC is complicated by a comparatively poor energy resolution (i.e., ~10 meV).[39] In contrast, the high energy resolution (~0.5 meV) of IR spectroscopy allows us to investigate the details of SPC by precise measurement of the phonon frequency shifts across the T_N.

Here, we report evidence for unconventional SPC via the DM interaction in $Y_2Ir_2O_7$. To investigate DM-derived SPC, we monitored the temperature (T)-dependent phonon spectra in $Y_2Ir_2O_7$ by infrared spectroscopy. Three IR-active phonons soften and sharpen below T_N, implying the presence of strong SPC. Based on first-principles calculations and tight-binding model analysis, we show that the observed phonon frequency shifts originate from the modulation of the Ir–O–Ir bond angle and establish that the phonon renormalization in $Y_2Ir_2O_7$ is predominantly driven by the DM interaction.

RESULTS

Phonon spectra measurement and Fano–Lorentz model analysis

In the present work, we investigated the IR-active phonons of a $Y_2Ir_2O_7$ polycrystalline sample. The photon energy range was $6 \le \hbar\omega \le 5{,}000$ meV and T ranged from 10 to 300 K. As presented in Fig. 2a, the $\sigma_1(\omega)$ spectra show seven IR-active phonons in $Y_2Ir_2O_7$[39–41] below 90 meV, as expected for the pyrochlore structure.[40,41] The experimental $\sigma_1(\omega)$ spectra also showed several weak peaks, possibly due to impurities,[42] but they did not influence our phonon analysis of $Y_2Ir_2O_7$. For later discussion, we label the seven strong phonon modes as Ph1 to Ph7 in order of increasing frequency, ω.

Three of the IR-active phonons exhibit an anomalous T-dependence. Figure 2b shows the T-dependent evolution of each phonon. The blue arrows show that Ph1, Ph2, Ph3, and Ph7 blueshift (i.e., harden) monotonically with decreasing T. On the other hand, the red arrows indicate that Ph4, Ph5, and Ph6 redshift (i.e., soften) abruptly. To perform a more quantitative analysis, we fitted the $\sigma_1(\omega)$ spectra with a Fano–Lorentz model. Figure 3a–c show that the $\omega_0(T)$ and $\Gamma(T)$ of Ph4, Ph5, and Ph6 show anomalous T-dependent changes near T_N. This behavior is in contrast with the smooth T-dependence of phonon parameters for Ph7 shown in Fig. 3d. (The parameters of other phonons are shown in Supplementary Note 1.)

A comparison with the phonon-phonon scattering theory can provide an insight into the phonon renormalization of $Y_2Ir_2O_7$. The red lines in Fig. 3 indicate the theoretical phonon frequencies, $\omega_0{}^{th}$, expected based on the simple phonon-phonon scattering theory.[27,43] The $\omega_0(T)$ of Ph7 is well-described by the theory. On the other hand, the $\omega_0(T)$ of Ph4, Ph5, and Ph6 show abrupt redshifts at $T_N \approx 170$ K that are not captured by the theory. For later discussion, we define the frequency difference, $\Delta\omega_0(T) \equiv \omega_0{}^{th}(T) - \omega_0(T)$ at $T = 10$ K. In addition, the $\Gamma(T)$ of Ph4, Ph5, and Ph6 also show kink-like features near T_N, as shown in the lower panels of Fig. 3a–c. The phonon linewidth, the inverse of the lifetime, can become smaller in the ordered state which is away from the phase transition. However, earlier XRD and neutron diffraction experiments showed that AIAO magnetic ordering in pyrochlore iridates is not accompanied by a structural transition.[44–46] Therefore, we can conclude that the anomalous T-dependence of Ph4, Ph5, and Ph6 should be coupled to the AIAO magnetic order.

Phonon analysis with density functional theory (DFT)

DFT calculations were performed to determine the phonon frequencies and corresponding eigenmodes of $Y_2Ir_2O_7$ (see Methods). The AIAO spin configuration of the pyrochlore structure was used for the calculations. These spins are aligned along the local Ir [111] axis in the Ir tetrahedra. Figure 4a shows the spin-canting angle $\theta_{\text{spin}} = \cos^{-1}\left(-\frac{1}{3}\right) \approx 109.5^\circ$ in the Ir–O–Ir plane,[47] which is marked as a blue area. Here, we choose the x_o- and z_o-axes of the local coordinates for O ions in the Ir–O–Ir plane, and the y_o-axis perpendicular to the plane. Our DFT calculations suggest that the Ir–O–Ir bond angle θ_0 is about 126.9°. This is close

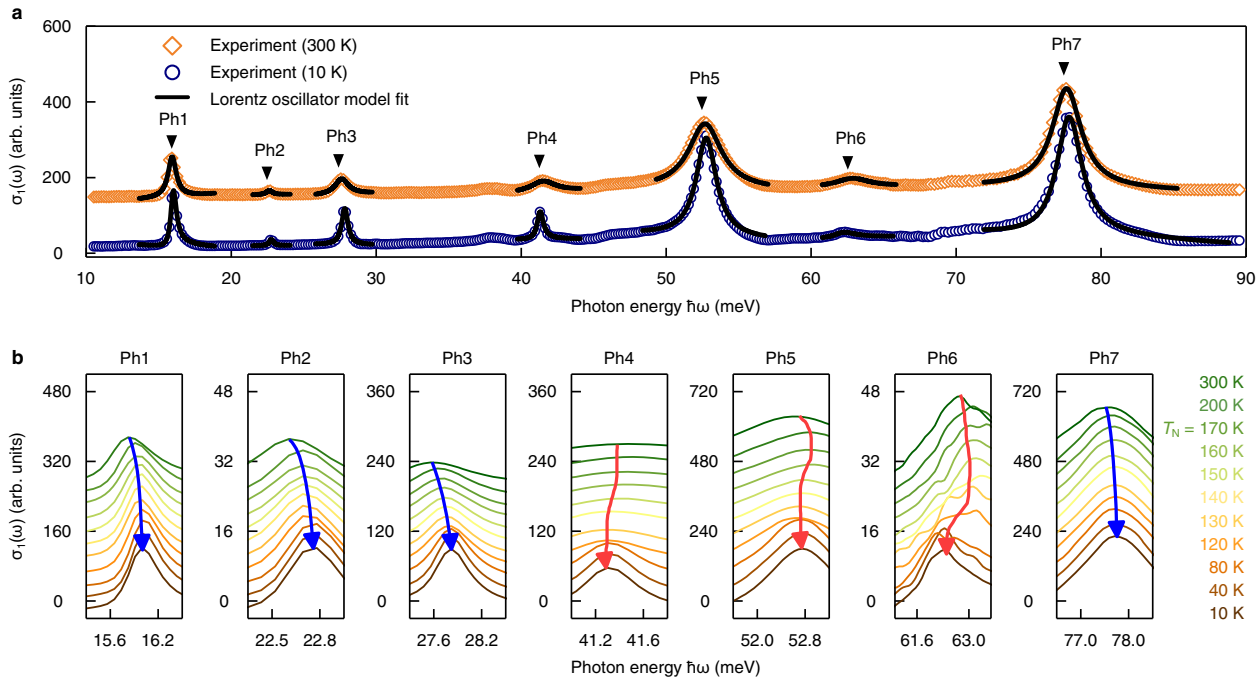

Fig. 2 *T*-dependent infrared (IR)-active phonons in $Y_2Ir_2O_7$. **a** The $\sigma_1(\omega)$ spectra at $T = 300$ K (orange diamonds) and 10 K (blue circles). The experimental $\sigma_1(\omega)$ were fitted using the Fano–Lorentz model (black solid lines), identifying seven IR-active phonon modes. The $\sigma_1(\omega)$ for each *T* has a vertical offset for clarity. **b** Evolution of all phonons as *T* varies from 300 K to 10 K. Vertical offsets are included for clarity. As *T* decreases, some phonons (Ph4, Ph5, and Ph6) exhibit a non-monotonic *T*-evolution of the peak energy (red arrows). The other phonons (Ph1, Ph2, Ph3, and Ph7) exhibit monotonic behavior (blue arrows).[27,43] T_N is approximately 170 K

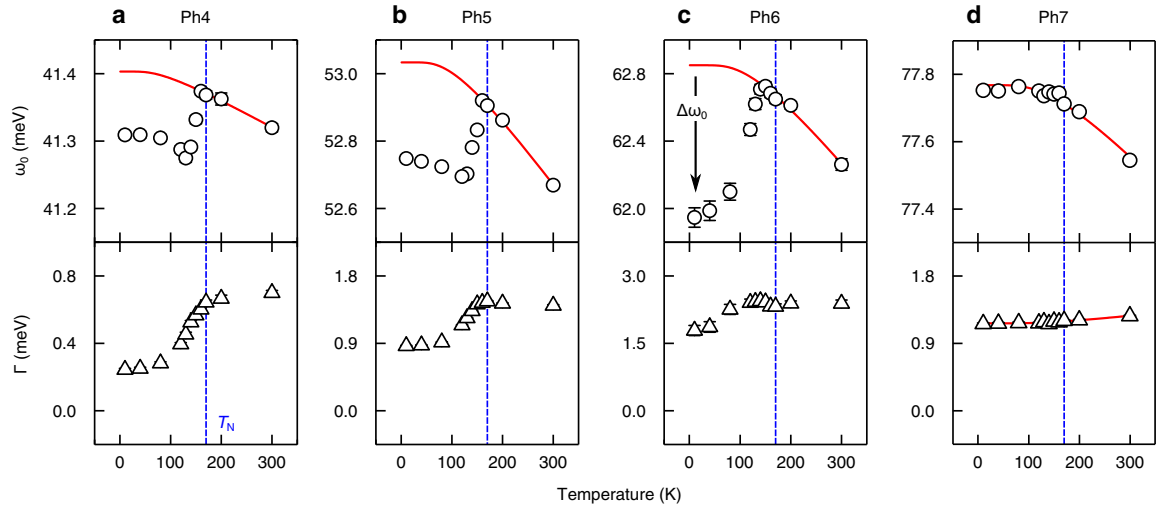

Fig. 3 *T*-dependence of phonon parameters, determined by the Fano–Lorentz model analysis. **a**–**d** *T*-dependent frequencies ω_0 and linewidths Γ from 10 to 300 K are shown. Blue dashed lines indicate T_N. Red solid lines indicate the ω_0 calculated from anharmonic phonon-phonon scattering theory ($\omega_0{}^{th}$ in the main text).[27,43] The anharmonic theory is parameterized so as to match the data at $T > T_N$. For three phonons (Ph4, Ph5, and Ph6), ω_0 deviates significantly from the red solid lines below T_N. The Γ of these same modes also reveal anomalies around T_N (for the parameters of other phonon modes, see Supplementary Note 1). On the other hand, the parameters of phonon (Ph7) do not show any anomalies and are well-described by the anharmonic phonon scattering theory

to the experimental values from 127.5° to 128.5° measured by neutron diffraction[44,48] and XRD,[49] respectively. As shown in Table 1, the DFT-calculated phonon frequencies agree well with the experimental values and therefore support the validity of our calculations.

To obtain further insight into the phonon renormalization, let us focus on the Ir–O–Ir bond. Note that O is the lightest element in $Y_2Ir_2O_7$, so its vibration amplitude should be largest. In this context, the motion of the O ion between the neighboring Ir spins plays an important role in the electron hopping along the Ir–O–Ir path and in H_{spin}.[13] The seven IR-active phonon modes can be classified into three categories based on the dominant motion of the O ions along the x_o-, y_o-, and z_o-directions (see Supplementary Note 2). The classification is shown in Fig. 4b: Ir–O–Ir stretching (Ph1 and Ph7), out-of-plane bending (Ph2, Ph3, and Ph4), and in-plane bending (Ph5 and Ph6) motion, respectively (see

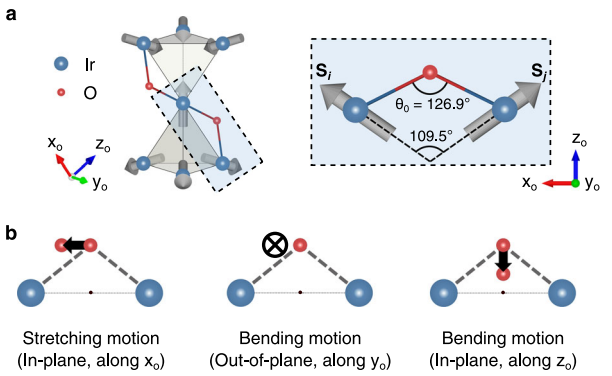

Fig. 4 All-in-all-out (AIAO) spin configurations (gray arrows), Ir–O–Ir bond of $Y_2Ir_2O_7$, and classification of phonon modes based on the O ion motion. **a** O ions (red spheres) are bonded to the nearest neighboring Ir ions (blue spheres) forming the Ir–O–Ir bond. In the AIAO magnetic order, the Ir spin-canting angle is about 109.5°. From first-principles calculations, the Ir–O–Ir bond angle θ_0 was estimated to be about 126.9°. **b** The IR-active phonons of $Y_2Ir_2O_7$ cause three types of O displacement. For the in-plane stretching mode, the O ion displacement is mostly along the x_o-axis, parallel to the Ir-Ir bond. For the out-of-plane bending mode, the O ion displacement is mostly along y_o-axis, perpendicular to the Ir–O–Ir plane. For the in-plane stretching mode, the O ion displacement is mostly along the z_o-axis in the Ir–O–Ir plane

Table 1. IR-active phonons determined via optical conductivity measurements at $T = 10$ K and DFT calculations

Label	Phonon frequency (meV)		Dominant motion of the Ir–O–Ir bond
	Experiment	DFT	
Ph1	15.98	15.29	Stretching
Ph2	22.76	22.17	Bending (out-of-plane)
Ph3	27.83	27.08	Bending (out-of-plane)
Ph4	41.31	40.06	Bending (out-of-plane)
Ph5	52.74	51.37	Bending (in-plane)
Ph6	62.41	63.32	Bending (in-plane)
Ph7	77.74	77.54	Stretching

DFT density functional theory

Supplementary Note 3). For the in-plane bending motion, the O displacement is parallel to the z_o-direction, making the associated θ change about 100 times larger than the other motions (see Supplementary Note 2). It should be noted that there are two kinds of O ions: one participating in the Ir–O–Ir bond and the other between Y ions (see Supplementary Note 3). In Ph5 and Ph6, O ions vibrate along the z_o-direction, as shown in Fig. 4b. For Ph6, all of the O ions in Ir–O–Ir bond participate in the in-plane vibrational motion. However, for Ph5, only one-third of O ions in the Ir–O–Ir bond participate. It makes the difference in the average change of angle θ between two distinct eigenmodes.

Based on the DFT results for the phonon eigenmodes, we estimated the change in the bond angle θ for each phonon mode. We assumed that the magnitude of the ionic displacements associated with each eigenmode is ~0.01 Å. Then, we calculated the concomitant bond angle change, $\Delta\theta \equiv \theta - \theta_0 = \theta - 126.9°$. The calculated $\Delta\theta/\theta_0$ ratios are plotted as a bar graph in Fig. 5. Note that $\Delta\theta/\theta_0$ becomes the largest for Ph6. The experimental $\Delta\omega_0/\omega_0$ ratios are also plotted as black squares. We found that $\Delta\omega_0/\omega_0$ and $\Delta\theta/\theta_0$ have similar trends. This behavior suggests that

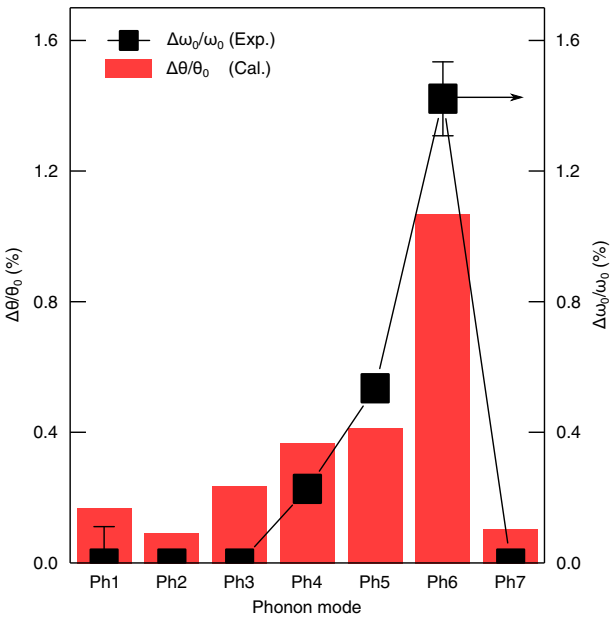

Fig. 5 Comparison between the phonon renormalization and calculation results. Relationship between the Ir–O–Ir bond angle change $\Delta\theta/\theta_0$ and the experimental phonon renormalization $\Delta\omega_0/\omega_0$ at 10 K. We calculated $\Delta\theta/\theta_0$ (red bars) using the ionic displacements obtained by DFT. We obtained the experimental $\Delta\omega_0/\omega_0$ (solid squares) from Fig. 3

the unusual phonon renormalization in $Y_2Ir_2O_7$ is closely related to the modulation of the Ir–O–Ir bond angle.

For conventional SPC, the bond length is the most critical parameter for modulating the IE interaction.[27,29,50] Change in the bond length may affect the overlap integral significantly, resulting in a sizable change in J_{IE}.[51] In $Y_2Ir_2O_7$, however, the Ir–O bond length change Δl has only a slight effect on $\Delta\omega_0$. We calculated the length changes $\Delta l/l_0$ associated with each phonon mode and found that they deviate markedly from the experimental results, especially for Ph4 and Ph7 (see Supplementary Note 4). Additionally, if Δl is indeed the critical parameter for the phonon renormalization, the stretching modes would be expected to show the largest frequency shift. However, the stretching mode Ph7 shows no frequency shift near T_N. These observations indicate that Δl cannot play important roles in $\Delta\omega_0$ at T_N.

Importance of the DM interaction for the phonon renormalization

To elucidate the microscopic origin of SPC in $Y_2Ir_2O_7$, we meticulously examined the relation between $\Delta\omega_0$ and $\Delta\theta$. The bond angle change induced by lattice vibration can affect the H_{spin} in $Y_2Ir_2O_7$, given in equation (1). Due to the strong SOC in pyrochlore iridates, the low energy magnetic degrees of freedom may be represented by pseudospins, $J_{eff} = 1/2$.[34,52] Due to the 1/2 value of J_{eff}, the SIA term becomes negligible.[53] Previous studies have also concluded that the AE interaction is at least an order of magnitude smaller than the other terms in H_{spin}.[13,54–56] Consequently, for $Y_2Ir_2O_7$, $\Delta\omega_0$ may be largely attributed to the IE and DM interactions:

$$\Delta\omega_0 \cong -\frac{2}{I\omega_0}\left(\sum_{i,j}^{nn}\frac{\partial^2 J_{IEij}(\theta)}{\partial\theta^2}\langle \mathbf{S}_i\cdot\mathbf{S}_j\rangle + \sum_{i,j}^{nn}\frac{\partial^2 \mathbf{D}_{ij}(\theta)}{\partial\theta^2}\cdot\langle \mathbf{S}_i\times\mathbf{S}_j\rangle\right), \quad (2)$$

where I is the rotational inertia of the given phonon[57] (see Supplementary Note 5 for derivation). The positive or negative sign of $\Delta\omega_0$ determines whether the corresponding phonon softens or hardens.

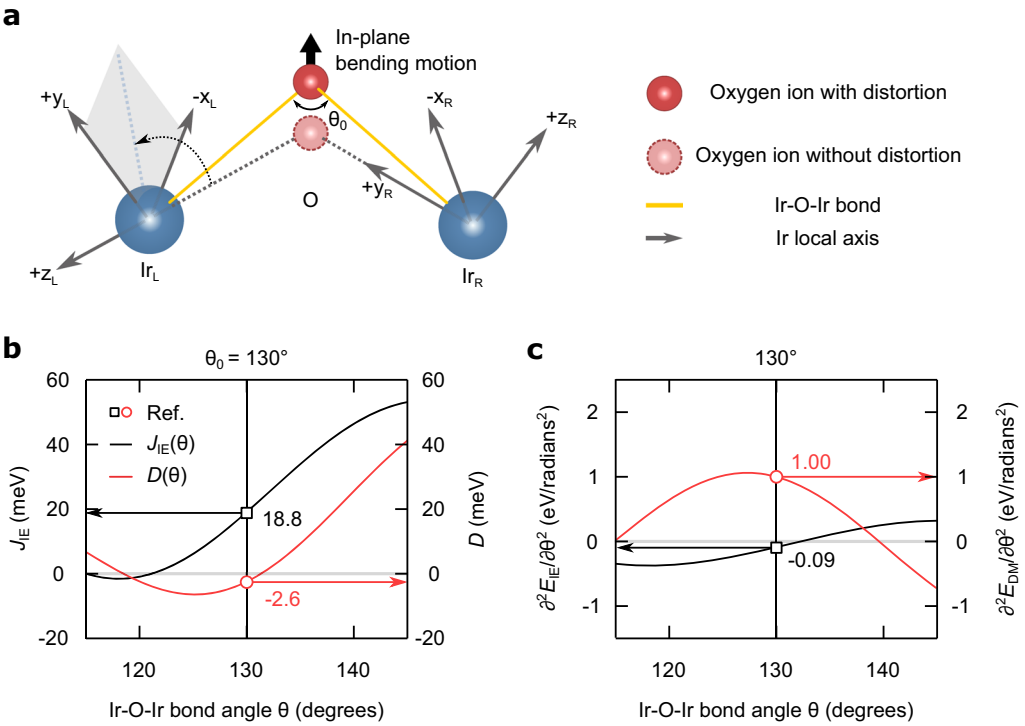

Fig. 6 Comparison between the IE and DM interaction contributions for SPC. **a** O-mediated hopping between the Ir sites. While maintaining the global lattice symmetry, the trigonal distortion of octahedra displaces the O ions from one of the Ir local axes. This O ion displacement direction is parallel to the in-plane bending motion. **b**, **c** The coefficients of the IE and DM interactions (J_{IE} and D), and their second derivatives of $E_{IE} = J_{IEij}(\theta)\langle S_i \cdot S_j\rangle$ and $E_{DM} = \mathbf{D}_{ij}(\theta)\cdot\langle \mathbf{S}_i \times \mathbf{S}_j\rangle$. Here we anchored the J_{IE} and D values at 130° using values from quantum chemistry calculations (see Supplementary Note 5).[60] Note that near $\theta = 130°$ the value of $\partial^2 E_{DM}/\partial\theta^2$ is an order of magnitude larger than that of $\partial^2 E_{IE}/\partial\theta^2$, implying the importance of the DM interaction for SPC

To compare the contributions of the IE and DM interactions quantitatively, we considered a tight-binding model based on O-mediated Ir-Ir hopping.[13] Previous tight-binding models for pyrochlore iridates assumed that Ir–O hopping could occur along the local axes.[13,54–56,58] However, the actual lattice structure includes a strong trigonal distortion of the O octahedra even though the global lattice symmetry is maintained. This distortion moves the O ion position away from the local axes of Ir ions (i.e., along the z_L and y_L axes in the Fig. 6a). Figure 6a show the changes of Ir–O–Ir bond during the trigonal distortion. Note that when the Ir–O–Ir bond angle changes to θ_0, the Ir–O hopping is no longer aligned to the local axes. With proper consideration of the ionic position changes, we analytically obtained the θ-dependent Ir–O–Ir hopping. Then, using the Slater-Koster tables, we derived the bond angle-dependent coefficients $J_{IE}(\theta)$ and $D(\theta)$ $(=\|\mathbf{D}_{ij}(\theta)\|)$ in H_{spin}[54–56,58,59] (see Supplementary Note 5 for derivation).

To make a quantitative comparison between $J_{IE}(\theta)$ and $D(\theta)$ for $Y_2Ir_2O_7$, we need to anchor their values for at least one angle. Unfortunately, experimental values have not yet been reported for $Y_2Ir_2O_7$. We therefore rely on a previous quantum chemistry calculation (QCC) study that computed $J_{IE}(\theta)$ (= 18.8 meV) and $D(\theta)$ (= 2.6 meV) at the experimentally determined angle θ_0^{QCC} (= 130°).[60,61] Using these QCC values, we quantitatively determined $J_{IE}(\theta)$ and $D(\theta)$, which are displayed in Fig. 6b.

Using the $J_{IE}(\theta)$ and $D(\theta)$ values, we then estimated the IE and DM interaction energies $E_{IE} = J_{IEij}(\theta)\langle \mathbf{S}_i \cdot \mathbf{S}_j\rangle$ and $E_{DM} = \mathbf{D}_{ij}(\theta)\cdot\langle \mathbf{S}_i \times \mathbf{S}_j\rangle$. By taking the second derivatives, i.e., the $\partial^2 E_{DM}/\partial\theta^2$ and $\partial^2 E_{IE}/\partial\theta^2$ curves shown in Fig. 6c, we can compare both the IE and DM contributions to $\Delta\omega_0$ using equation (22). The results suggest $\partial^2 E_{DM}/\partial\theta^2 \approx 1.00$ eV/radians^2 and $\partial^2 E_{IE}/\partial\theta^2 \approx -0.09$ eV/radians^2 at $\theta = 130°$. The contribution to phonon renormalization of the DM interaction ($\partial^2 E_{DM}/\partial\theta^2$) is therefore about an order of magnitude greater than that of the IE interaction ($\partial^2 E_{IE}/\partial\theta^2$). The dominance of the DM interaction is robust even when the anchoring values of $J_{IE}(\theta)$ and $D(\theta)$ were varied significantly. The DM interaction therefore plays a key role in the unconventional SPC observed in $Y_2Ir_2O_7$.

DISCUSSION

We now discuss the importance of the bond angle, as this determines the dominant SPC mechanism. For the IE interaction, we can empirically write $J_{IE}(\theta) = J_{90°}\sin^2\theta + J_{180°}\cos^2\theta$, where $J_{90°}$ and $J_{180°}$ represent the IE interaction terms from the bond angles 90° and 180°, respectively.[62] Using a Taylor expansion, $J_{IE}(\theta)$ becomes an approximately linear function of θ around 135°. And as a result, the SPC due to the IE interaction (i.e., $\partial^2 E_{IE}/\partial\theta^2$) is strongly suppressed with $\theta \sim 135°$. In contrast, the DM interaction is expected to vary as $\sin(2\theta)$,[63] meaning $\partial^2 E_{DM}/\partial\theta^2$ is zero at 180° and a maximum near 135°. Therefore, the DM interaction can play a dominant role in driving the SPC when θ is close to 135°.

To obtain a better perspective, we now compare the phonon renormalization of $Y_2Ir_2O_7$ to that of two other 5*d* TMOs: $NaOsO_3$ and $Ca_2Os_2O_7$. The relevant physical parameters are summarized in Table 2.[11,50,60,61,64,65] Recently, Calder et al. reported that the breathing phonon mode of $NaOsO_3$ has $\Delta\omega_0$~5.0 meV, the largest observed in solids.[50] This large renormalization was attributed to the strong modulation of the IE interaction by the Os–O-Os bond stretching motion. Indeed, $NaOsO_3$ has a distorted perovskite structure and θ is close to 180°. Following our earlier arguments regarding θ, the IE interaction is expected to be the leading contributor to the SPC. The SPC mechanism in $NaOsO_3$ may therefore be distinguished from that of $Y_2Ir_2O_7$ due to different bond angles in the two compounds.

We now turn to the SPC occurring in $Cd_2Os_2O_7$, a compound that shares the same crystal structure and magnetic ground state

Table 2. Physical parameters for 5*d* transition metal oxides: iridate and osmates

Materials	Spin interaction (meV)			θ (degrees)	Max. $\Delta\omega_0$ (meV)	Main cause for SPC
	DM	SIA	IE			
$Y_2Ir_2O_7$[60,61]	2.6	–	18.8	130	1.2	DM interaction
$NaOsO_3$[51,64]	–	4.0	13.9	155	5.0	IE interaction
$Cd_2Os_2O_7$[11,65]	1.7	−6.8	6.4	137	3.0	SIA

DM Dzyaloshinskii–Moriya, *SIA* single-ion anisotropy, *IE* isotropic exchange, *SPC* spin-phonon coupling

as $Y_2Ir_2O_7$. Sohn et al. reported a huge phonon hardening below T_N in $Cd_2Os_2O_7$[11] and attributed it to the SPC via the SIA. The SIA energy can change rapidly with the trigonal distortion of the OsO_6 octahedra and so is especially sensitive to phonons that modulate this distortion.[11,65] In contrast, in $Y_2Ir_2O_7$, we can neglect the SIA term because of $J_{eff} = 1/2$, as shown in equation (22). It is also of interest to note that, despite their structural and magnetic similarities, $Cd_2Os_2O_7$ and $Y_2Ir_2O_7$ reveal opposite signs of $\Delta\omega_0$ due to the different origins of the SPC.

In summary, we have established DM-mediated strong SPC in $Y_2Ir_2O_7$ using both IR spectroscopy and first-principles calculations. Remarkable variations in the phonon parameters (frequency and linewidth) were observed near T_N. These changes can be understood in terms of the change in Ir–O–Ir bond angle induced by the relevant phonon. We also explained that the dynamic modulation of the DM interaction is maximized in materials with large SOC and Ir–O–Ir angle close to 135°. We expect that similar phenomena should be observed in other materials with large SOC and highly non-collinear spin ground states.

METHODS

Synthesis

We obtained a high-quality polycrystalline $Y_2Ir_2O_7$ sample using Y_2O_3 (99.999%; Alfa Aesar) and IrO_2 (99.9%; Sigma Aldrich) powders. As IrO_2 evaporates easily during sintering, we used 4–10% more IrO_2 than suggested by the stoichiometric ratio, Y_2O_3: IrO_2 = 1:2. The mixture was pelletized and calcinated in a box furnace at 760 °C for 48 h. After re-grinding and re-pelletizing, several annealing cycles were performed at temperatures between 900 °C and 1030 °C, each for 48 h. High-density targets were prepared for optical experiments by pelletizing $Y_2Ir_2O_7$ powder using a high-pressure anvil (NCAP-035; Nanki Engineering) operating at 4.3 GPa. Samples with densities >87% were polished to render the surfaces shiny and flat (see Supplementary Note 6 for details).

X-ray diffraction measurement

XRD was used to verify the quality of our $Y_2Ir_2O_7$ crystals, as outlined below. Powder XRD data were obtained using a high-resolution powder diffractometer (D8 Discover; Bruker) operating at wavelengths of 1.54590 and 1.544310 Å ($K_{\alpha1}$ and $K_{\alpha2}$, respectively).

Optical conductivity fitting

We measured the near-normal reflectance spectra $R(\omega)$ by Fourier transform infrared spectroscopy (VERTEX 80 v; Bruker) and spectroscopic ellipsometry (V-VASE; J.A. Woollam). To compensate for the effects of rough surface, we normalized $R(\omega)$ relative to those measured after *in-situ* gold evaporation.[66] From $R(\omega)$, we calculated the optical conductivity spectra, $\tilde{\sigma}(\omega) = \sigma_1(\omega) + i\sigma_2(\omega)$ using the Kramers-Kronig transformation. To track the spectral components, we fitted $\sigma_1(\omega)$ to a Fano–Lorentz line shape, given by

$$\sigma_1(\omega) = \frac{SW}{4\pi\Gamma}\frac{q^2+2q\epsilon-1}{q^2(1+\epsilon^2)}, \quad (3)$$

where ω is the angular frequency of the photon, $\epsilon = (\omega - \omega_0)/\Gamma$ is a dimensionless parameter for reduced energy, and q is the Fano asymmetry parameter. Here, ω_0, Γ, and $SW = 8\int\sigma_1(\omega')d\omega'$ are the resonance frequency, linewidth, and spectral weight of the phonon, respectively. For the data measured at 10 and 300 K, the fitted curves are presented as black solid lines in Fig. 2a (for more detailed information, see Supplementary Note 1).

DFT calculations

To obtain the phonon eigenmodes of $Y_2Ir_2O_7$, we performed DFT+U calculations with the PBEsol exchange correlation function implemented in VASP.[67] We chose the effective $U = 1.5$ eV to simulate the local Hubbard interaction of Ir,[35] and used the non-collinear DFT formalism to express the AIAO magnetic configuration. We fully optimized the lattice structure and obtained Ir–O–Ir angle $\theta_0 \approx 126.9°$, as shown in Fig. 4b. We calculated the zone-center phonon modes using the frozen-phonon method. The resulting phonon eigenmodes are summarized in Supplementary Note 3.

Tight-binding model analysis

Using a tight-binding model, we derived $J_{IE}(\theta)$ and $D(\theta)$, which were required to calculate $\Delta\omega_0$ in equation (22). We derived the effective hopping Hamiltonian, based on the model of Pesin and Balents.[13] However, we applied the effects of strong trigonal distortion of octahedra. We considered two types of electron hopping between the nearest neighbor Ir ions: namely, O-mediated Ir-Ir hopping t_{oxy} and direct Ir-Ir hopping t_σ. With $t(\theta) = a(\theta)\, t_{oxy} + b\, t_\sigma$ and $v(\theta) = a'(\theta)\, t_{oxy} + b'\, t_\sigma$, we could derive the IE and DM interaction: $J_{IE} = \frac{4}{U}\left(t^2(\theta) - \frac{1}{3}v^2(\theta)\right)$ and $D = \frac{8}{U}t(\theta)v(\theta)$. The coefficients $a(\theta)$, b, $a'(\theta)$, and b' were obtained using the Slater-Koster method[59] (see Supplementary Note 5). We estimated the values of t_{oxy} and t_σ by anchoring with the reported values ($J_{IE} = 18.8$ meV and $D = 2.6$ meV at $\theta_0^{QCC} = 130°$) obtained from quantum chemistry calculation (QCC).[60] The calculated $J_{IE}(\theta)$ and $D(\theta)$ are presented in Fig. 6b.

DATA AVAILABILITY

All relevant data that support the findings of this study are available from the corresponding author on request.

ACKNOWLEDGEMENTS

We gratefully acknowledge useful discussions with K. W. Kim. This work was mainly supported by the Institute for Basic Science (IBS) in Korea (Grant No. IBS-R009-D1 and IBS-R009-G1). S. J. Moon was supported by Basic Science Research Program through the National Research Foundation of Korea (NRF) funded by the Ministry of Science, ICT and Future Planning (Grant No. NRF-2017R1A2B4009413). S. Y. Kim was supported by the Global Ph.D. Fellowship Program through NRF funded by the Ministry of Education (Grant No. NRF-2015H1A2A1034943).

AUTHOR CONTRIBUTIONS

J.S., S.J.M., and T.W.N. conceived and designed the project; H.B.C. prepared the polycrystalline sample under the supervision of J.G.P; J.S., and S.Y.K. performed FT-IR measurements under the supervision of L.J.S. and S.J.M; C.H.K. performed DFT calculations; J.S. analyzed optical spectroscopy data under the supervision of C.H.S., C. H.K., B.C.P., and T.W.N; J.S., B.C.P., C.H.K., and T.W.N. wrote the paper. All authors discussed the results and commented on the manuscript.

ADDITIONAL INFORMATION

Supplementary information accompanies the paper on the *npj Quantum Materials* website (https://doi.org/10.1038/s41535-019-0157-0).

Competing interests: The authors declare no competing interests.

Publisher's note: Springer Nature remains neutral with regard to jurisdictional claims in published maps and institutional affiliations.

REFERENCES

1. Khomskii, D. I. & Sawatzky, G. A. Interplay between spin, charge and orbital degrees of freedom in magnetic oxides. *Solid State Commun.* **102**, 87–99 (1997).

2. Orenstein, J. & Millis, A. J. Advances in the physics of high-temperature superconductivity. *Science* **288**, 468–475 (2000).
3. Lanzara, A. et al. Evidence for ubiquitous strong electron-phonon coupling in high-temperature superconductors. *Nature* **412**, 510–514 (2001).
4. Tokura, Y. & Nagaosa, N. Orbital physics in transition-metal oxides. *Science* **288**, 462–468 (2000).
5. Eerenstein, W., Mathur, N. D. & Scott, J. F. Multiferroic and magnetoelectric materials. *Nature* **442**, 759–765 (2006).
6. Lee, J. H. et al. A strong ferroelectric ferromagnet created by means of spin-lattice coupling. *Nature* **466**, 954–958 (2010).
7. Mochizuki, M., Furukawa, N. & Nagaosa, N. Theory of spin-phonon coupling in multiferroic manganese perovskites $R$$MnO_3$. *Phys. Rev. B* **84**, 144409 (2011).
8. Moya, X. & Mathur, N. D. Thermal hall effect: Turn your phonon. *Nat. Mater.* **16**, 784–785 (2017).
9. Calero, C., Chudnovsky, E. M. & Garanin, D. A. Field dependence of the electron spin relaxation in quantum dots. *Phys. Rev. Lett.* **95**, 166603 (2005).
10. Ramesh, R. & Spaldin, N. A. Multiferroics: progress and prospects in thin films. *Nat. Mater.* **6**, 21–29 (2007).
11. Sohn, C. H. et al. Strong spin-phonon coupling mediated by single ion anisotropy in the all-in-all-out pyrochlore magnet $Cd_2Os_2O_7$. *Phys. Rev. Lett.* **118**, 117201 (2017).
12. Nguyen, T. M. H. et al. Two-magnon scattering in the 5*d* all-in-all-out pyrochlore magnet $Cd_2Os_2O_7$. *Nat. Commun.* **8**, 251 (2017).
13. Pesin, D. & Balents, L. Mott physics and band topology in materials with strong spin–orbit interaction. *Nat. Phys.* **6**, 376–381 (2010).
14. Moriya, T. Anisotropic superexchange interaction and weak ferromagnetism. *Phys. Rev.* **120**, 91–98 (1960).
15. Jin, H., Jeong, H., Ozaki, T. & Yu, J. Anisotropic exchange interactions of spin-orbit-integrated states in Sr_2IrO_4. *Phys. Rev. B* **80**, 075112 (2009).
16. Kittel C. & McEuen P. *Introduction to Solid State Physics* 8th edn, (Wiley, New York, 1996).
17. Lee, S. et al. Giant magneto-elastic coupling in multiferroic hexagonal manganites. *Nature* **451**, 805–808 (2008).
18. Laverdière, J. et al. Spin-phonon coupling in orthorhombic $R$$MnO_3$ (R=Pr, Nd, Sm, Eu, Gd, Tb, Dy, Ho, Y): A Raman study. *Phys. Rev. B* **73**, 214301 (2006).
19. Granado, E. et al. Dramatic changes in the magnetic coupling mechanism for la-doped $CaMnO_3$. *Phys. Rev. Lett.* **86**, 5385–5388 (2001).
20. Issing, S., Pimenov, A., Ivanov, V. Y., Mukhin, A. A. & Geurts, J. Composition-dependent spin-phonon coupling in mixed crystals of the multiferroic manganite $Eu_{1-x}Y_xMnO_3$ ($0 \le x \le 0.5$) studied by Raman spectroscopy. *Phys. Rev. B* **81**, 024304 (2010).
21. Mota, D. A. et al. Competing exchanges and spin-phonon coupling in $Eu_{1-x}R_xMnO_3$ (R=Y, Lu). *J. Phys.: Condens. Matter* **25**, 235602 (2013).
22. Petit, S. et al. Spin phonon coupling in hexagonal multiferroic $YMnO_3$. *Phys. Rev. Lett.* **99**, 266604 (2007).
23. Sakai, H. et al. Soft phonon mode coupled with antiferromagnetic order in incipient-ferroelectric Mott insulators $Sr_{1-x}Ba_xMnO_3$. *Phys. Rev. B* **86**, 104407 (2012).
24. Sushkov, A. B., Tchernyshyov, O., Ratcliff, W. II, Cheong, S. W. & Drew, H. D. Probing spin correlations with phonons in the strongly frustrated magnet $ZnCr_2O_4$. *Phys. Rev. Lett.* **94**, 137202 (2005).
25. Bordács, S. et al. Magnetic-order-induced crystal symmetry lowering in ACr_2O_4 ferrimagnetic spinels. *Phys. Rev. Lett.* **103**, 077205 (2009).
26. Kant, C. et al. Optical phonons, spin correlations, and spin-phonon coupling in the frustrated pyrochlore magnets $CdCr_2O_4$ and $ZnCr_2O_4$. *Phys. Rev. B* **80**, 214417 (2009).
27. Lee, J. S. et al. Strong spin-phonon coupling in the geometrically frustrated pyrochlore $Y_2Ru_2O_7$. *Phys. Rev. B* **69**, 214428 (2004).
28. Silverstein, H. J. et al. Liquidlike correlations in single-crystalline $Y_2Mo_2O_7$: An unconventional spin glass. *Phys. Rev. B* **89**, 054433 (2014).
29. Cazorla, C., Dieguez, O. & Iniguez, J. Multiple structural transitions driven by spin-phonon couplings in a perovskite oxide. *Sci. Adv.* **3**, e1700288 (2017).
30. Cheong, S.-W. & Mostovoy, M. Multiferroics: a magnetic twist for ferroelectricity. *Nat. Mater.* **6**, 13–20 (2007).
31. Fiebig, M., Lottermoser, T., Meier, D. & Trassin, M. The evolution of multiferroics. *Nat. Rev. Mater.* **1**, 16046 (2016).
32. Wan, X., Turner, A. M., Vishwanath, A. & Savrasov, S. Y. Topological semimetal and Fermi-arc surface states in the electronic structure of pyrochlore iridates. *Phys. Rev. B* **83**, 205101 (2011).
33. Shanavas, K. V., Popović, Z. S. & Satpathy, S. Theoretical model for Rashba spin-orbit interaction in d electrons. *Phys. Rev. B* **90**, 165108 (2014).
34. Kim, B. J. et al. Novel $J_{\rm eff}$ = 1/2 mott state induced by relativistic spin-orbit coupling in Sr_2IrO_4. *Phys. Rev. Lett.* **101**, 076402 (2008).
35. Disseler, S. M. Direct evidence for the all-in/all-out magnetic structure in the pyrochlore iridates from muon spin relaxation. *Phys. Rev. B* **89**, 140413(R) (2014).
36. Arima, T.-h Time-reversal symmetry breaking and consequent physical responses induced by All-In-All-Out type magnetic order on the pyrochlore lattice. *J. Phys. Soc. Jpn.* **82**, 013705 (2013).
37. Oh, J. et al. Spontaneous decays of magneto-elastic excitations in non-collinear antiferromagnet (Y, Lu)MnO_3. *Nat. Commun.* **7**, 13146 (2016).
38. Xiong, Z., Datta, T., Stiwinter, K. & Yao, D.-X. Magnon-phonon coupling effects on the indirect *K*-edge resonant inelastic x-ray scattering spectrum of a two-dimensional Heisenberg antiferromagnet. *Phys. Rev. B* **96**, 144436 (2017).
39. Ament, L. J. P., Khaliullin, G. & van den Brink, J. Theory of resonant inelastic x-ray scattering in iridium oxide compounds: Probing spin-orbit-entangled ground states and excitations. *Phys. Rev. B* **84**, 020403(R) (2011).
40. Vandenborre, N. T., Husson, E. & Brusset, H. Analyse en coordonnées normales des composés $A_2^{III}B_2^{IV}O_7$ (A = La, Nd; B = Zr, Hf) de structure pyrochlore. *Spectrochim. Acta A* **37**, 113–118 (1981).
41. Kumar, S. & Gupta, H. C. First principles study of zone centre phonons in rare-earth pyrochlore titanates, $RE_2Ti_2O_7$ (RE = Gd, Dy, Ho, Er, Lu; Y). *Vib. Spectrosc.* **62**, 180–187 (2012).
42. Schaack, G. & Koningstein, J. A. Phonon and electronic raman spectra of cubic rare-earth oxides and isomorphous yttrium oxide. *J. Opt. Soc. Am.* **60**, 1110–1115 (1970).
43. Menéndez, J. & Cardona, M. Temperature dependence of the first-order Raman scattering by phonons in Si, Ge, and α-Sn: Anharmonic effects. *Phys. Rev. B* **29**, 2051–2059 (1984).
44. Shapiro, M. C. et al. Structure and magnetic properties of the pyrochlore iridate $Y_2Ir_2O_7$. *Phys. Rev. B* **85**, 214434 (2012).
45. Clancy, J. P. et al. X-ray scattering study of pyrochlore iridates: crystal structure, electronic, and magnetic excitations. *Phys. Rev. B* **94**, 024408 (2016).
46. Takatsu, H., Watanabe, K., Goto, K. & Kadowaki, H. Comparative study of low-temperature x-ray diffraction experiments on $R_2Ir_2O_7$ (R = Nd, Eu, and Pr). *Phys. Rev. B* **90**, 235110 (2014).
47. Dai, D. & Whangbo, M. H. Classical spin and quantum-mechanical descriptions of geometric spin frustration. *J. Chem. Phys.* **121**, 672–680 (2004).
48. Clancy, P., Yamani, Z., Donaberger, R. & Kim, Y. *Searching for Magnetic Order in the Pyrochlore Iridate* $Y_2Ir_2O_7$ http://cins.ca/docs/exp_rep/CNBC-2012-QM-1.pdf (2012).
49. Kumar, H. & Pramanik, A. K. Glass-like behavior in pyrochlore iridate $Y_2Ir_2O_7$. *AIP Conf. Proc.* **1731**, 130053 (2016).
50. Calder, S. et al. Enhanced spin-phonon-electronic coupling in a 5*d* oxide. *Nat. Commun.* **6**, 8916 (2015).
51. Wan, X., Ding, H.-C., Savrasov, S. Y. & Duan, C.-G. Short range magnetic exchange interaction favors ferroelectricity. *Sci. Rep.* **6**, 22743 (2016).
52. Clancy, J. P. et al. Spin-orbit coupling in iridium-based 5*d* compounds probed by x-ray absorption spectroscopy. *Phys. Rev. B* **86**, 195131 (2012).
53. Shinaoka, H., Miyake, T. & Ishibashi, S. Noncollinear magnetism and spin-orbit coupling in 5d pyrochlore oxide $Cd_2Os_2O_7$. *Phys. Rev. Lett.* **108**, 247204 (2012).
54. Witczak-Krempa, W. & Kim, Y. B. Topological and magnetic phases of interacting electrons in the pyrochlore iridates. *Phys. Rev. B* **85**, 045124 (2012).
55. Witczak-Krempa, W., Go, A. & Kim, Y. B. Pyrochlore electrons under pressure, heat, and field: Shedding light on the iridates. *Phys. Rev. B* **87**, 155101 (2013).
56. Lee, E. K.-H., Bhattacharjee, S. & Kim, Y. B. Magnetic excitation spectra in pyrochlore iridates. *Phys. Rev. B* **87**, 214416 (2013).
57. Granado, E. et al. Magnetic ordering effects in the Raman spectra of $La_{1-x}Mn_{1-x}O_3$. *Phys. Rev. B* **60**, 11879–11882 (1999).
58. Yang, B.-J. & Kim, Y. B. Topological insulators and metal-insulator transition in the pyrochlore iridates. *Phys. Rev. B* **82**, 085111 (2010).
59. Slater, J. C. & Koster, G. F. Simplified LCAO method for the periodic potential problem. *Phys. Rev.* **94**, 1498–1524 (1954).
60. Yadav, R. et al. Heavy-mass magnetic modes in pyrochlore iridates due to dominant Dzyaloshinskii-Moriya interaction. *Phys. Rev. Mater.* **2**, 074408 (2018).
61. Taira, N., Wakeshima, M. & Hinatsu, Y. Magnetic properties of iridium pyrochlores $R_2Ir_2O_7$ (R = Y, Sm, Eu and Lu). *J. Phys.: Condens. Matter* **13**, 5527–5533 (2001).
62. Motida, K. & Miyahara, S. On the 90° exchange interaction between cations (Cr^{3+}, Mn^{2+}, Fe^{3+} and Ni^{2+}) in oxides. *J. Phys. Soc. Jpn.* **28**, 1188–1196 (1970).
63. Kim, B. H., Khaliullin, G. & Min, B. I. Magnetic couplings, optical spectra, and spin-orbit exciton in 5*d* electron Mott insulator Sr_2IrO_4. *Phys. Rev. Lett.* **109**, 167205 (2012).
64. Calder, S. et al. Strongly gapped spin-wave excitation in the insulating phase of $NaOsO_3$. *Phys. Rev. B* **95**, 020413 (2017).
65. Bogdanov, N. A., Maurice, R., Rousochatzakis, I., van den Brink, J. & Hozoi, L. Magnetic state of pyrochlore $Cd_2Os_2O_7$ emerging from strong competition of ligand distortions and longer-range crystalline anisotropy. *Phys. Rev. Lett.* **110**, 127206 (2013).
66. Homes, C. C., Reedyk, M., Cradles, D. A. & Timusk, T. Technique for measuring the reflectance of irregular, submillimeter-sized samples. *Appl. Opt.* **32**, 2976–2983 (1993).

67. Kresse, G. & Hafner, J. *Ab initio* molecular dynamics for open-shell transition metals. *Phys. Rev. B* **48**, 13115–13118 (1993).